



# Effects of build orientation and heat treatment on microstructure, mechanical and corrosion properties of Al6061 aluminium parts built by cold spray additive manufacturing process

Novana Hutasoit<sup>a,b</sup>, Muhammad Awais Javed<sup>a,c</sup>, Rizwan Abdul Rahman Rashid<sup>a,b</sup>, Scott Wade<sup>a,c</sup>, Suresh Palanisamy<sup>a,b,c,\*</sup>

<sup>a</sup> School of Engineering, Swinburne University of Technology, Hawthorn, VIC 3122, Australia

<sup>b</sup> DMTC Limited, Hawthorn, Victoria 3122, Australia

<sup>c</sup> Defence Science Institute, Carlton, Victoria, Australia



## ARTICLE INFO

**Keywords:**  
Cold spray additive manufacturing  
Aluminium  
Mechanical properties  
Corrosion  
Heat treatment  
Anisotropy

## ABSTRACT

Aluminium 6061 alloy (Al6061) is one of the widely used materials in the aluminium alloy family for structural applications owing to its high strength-to-weight ratio and high corrosion resistance. Al6061 components are traditionally manufactured using conventional processes such as casting, forging, rolling, and machining, which typically involved high scrap/waste generation. However, with the advent of advanced additive manufacturing (AM) processes, there is an opportunity to reconsider component design to near-net shapes with reduced material wastage. Although mechanical and corrosion properties of Al6061 fabricated with conventional processes is well understood, very little information is known about AMed Al6061. This study investigates the effect of build orientation and heat treatment on the mechanical and corrosion properties of Al6061 samples manufactured by cold spray additive manufacturing (CSAM) process. To the best of the authors' knowledge, this work is the first to explore both the mechanical and corrosion properties of Al6061 alloy print-parts fabricated using this unique CSAM system. Due to the lack of metallurgical bonding between powder particles, as-deposited samples - regardless of their build orientation, exhibited lower strength and ductility compared to the wrought counterparts. Particle shape generated by cold spray process exhibits an influence on the strength of horizontally and vertically build deposits. Expectedly, heat treatment significantly improved the mechanical properties by inducing metallurgical bonding at prior particle boundaries. As for corrosion resistance, horizontally-built samples exhibited the highest pit depth and pit penetration rate compared to the other conditions, which suggested a higher susceptibility to pitting corrosion owing to more strain-hardened particle sites available for corrosive attack. Heat treatment on as-deposited samples produced strain-free grains; thus, eliminating areas prone to corrosive environmental attack, leading to improvement in pitting corrosion resistance. Investigating post-processing heat treatment is crucial to improve the mechanical properties of as-deposited samples to a level similar to the ones of wrought condition. This research work is essential for selecting the correct processing routes and their parameters to manufacture components exposed to corrosive environments.

## 1. Introduction

Aluminium 6061 alloy (Al6061) is known for its high strength-to-weight ratio and therefore widely used for structural applications in aerospace and automotive industries [1,2]. It also has high corrosion resistance owing to the formation of a thin passive oxide layer over its surface [3]. This property enables Al6061 to be widely used in applications exposed to marine environments [4].

The recent advancement in metal additive manufacturing (AM) has triggered a shift from the conventional subtractive approach (i.e. cast-

ing and machining) that has been used as the primary manufacturing route for many decades [5-8]. By using this new approach, manufacturing structural components made of metals have been explored. Several studies have reported promising results from applying AM technology, mainly through selective laser melting (SLM) for manufacturing aluminium alloys [9-12]. This technique is considered one of the most economical AM processes to fabricate cellular and lattice structure components [13-17]. For Al6061, in conjunction with powder bed preheating and post-build heat treatment, SLM is capable of manufacturing parts with a higher yield and tensile strength, however, with lower

\* Corresponding author: School of Engineering, Swinburne University of Technology, Hawthorn, VIC 3122, Australia.

E-mail address: [spalanisamy@swin.edu.au](mailto:spalanisamy@swin.edu.au) (S. Palanisamy).

**Table 1**

Chemical composition of as-received wrought and powder Al6061 measured by X-ray fluorescence (XRF).

	Composition (wt.%)									
	Al	Mg	Si	Fe	Cu	Cr	Zn	Ti	Mn	Other
Wrought Al6061	97.74	0.75	0.64	0.357	0.173	0.054	0.103	0.059	0.1	0.024
Al6061 powder	97.89	0.9	0.43	0.115	0.356	0.286	0.0102	-	-	0.0128

ductility compared to the wrought counterparts [18]. Similarly, Ahmed et al. [19] reported that effective powder bed preheating is crucial in reducing cracking susceptibility during SLM processing of Al6061. Despite the promising results, SLM technology poses a challenge to fabricate aluminium alloys due to the formation of porosity, balling effect, high-temperature oxidation and other undesirable defects [20-22].

A more recent development in the AM landscape is cold spray additive manufacturing (CSAM) process developed as a coating's technology several decades ago [23]. More recently this technology is used to apply copper coatings on high-touch surfaces to inactivate harmful viruses [24]. This process involves spraying metal powder particles with high kinetic energies onto a substrate to fabricate 3D shapes and contours [25]. Since this technology does not induce bulk melting, it is therefore capable of overcoming the problem associated with high-temperature processing such as phase transformation and oxidation [26,27]. In this method of material deposition, micro-sized particles are increased to supersonic velocity in a nozzle by compressed inert gas namely, air, He or N<sub>2</sub> with low temperatures (<1000 °C) and deposit onto the substrate. The particles diameters range from 5 to 40 nm with a high pressure 10–60 bar and with He or N<sub>2</sub> as a medium. This inert gas medium helps in rapid cooling to -100 °C to +100 °C therefore the particles do not attain melting point [28]. Due to high velocities at the time of deposition the particles undergo plastic deformation on impact where the particles bond with the surface [29].

As-deposited cold spray deposits generally consist of inferior mechanical properties in comparison to bulk materials as they carry defects within the deposits. When the impact velocity of the particle is low the effect of brittle and no ductility are prominent [30]. Apart from the mechanical properties, electrical conductivity and thermal conductivity are lower when in comparison to the bulk material due to the defects in the deposits which avoids the flow of current and heat between the deposits [31]. As-deposited material generally exhibit hardness greater than that of bulk materials due to hardening effect during deposition process [32]. The as-deposited material shows improved mechanical properties when fabricated using high particle impact velocities and also higher strength compared to annealed deposits and bulk materials.

Cold spray deposits which undergo heat treatment tend to show the most effective properties. Annealing the as-deposited materials can improve strength and ductility of the material significantly due to the reduction of defects [33]. The elongation and strength of the annealed copper under proper conditions can obtain the same properties as the bulk copper and improve the elastic modulus due to the reduction of defects [34]. Annealed copper deposits tend to have better thermal and electrical conductivity due to the repaired boundaries for the flow of heat and current [35,36].

Several studies by Rokni et al. [37-40] reported the application of cold spray technology in manufacturing Al6061 coatings of several millimetres in thickness. Using helium as carrier gas during the process followed by post-processing heat treatment, Rokni et al. showed a significant improvement in the strength of cold sprayed Al6061 coatings, to a level higher than wrought Al6061 (T6 temper). Furthermore, corrosion properties of Al6061 coatings were also investigated [41]. The surface of an additively manufactured alloy is usually defective in nature as it comes with a covered oxide scale and these act as promoters for crevice corrosion. This oxide scale is chemically and structurally different from the native oxide as those formed in corrosive passive metals. This can be very thick and be further trapped as oxide inclusions into

the microstructure. This oxide can be protective if it's dense and well-structured, but the rapid manufacturing is associated with a large in built dislocation density that is similar to a highly deformed microstructure [42]. Although preliminary research on cold sprayed Al6061 coatings have shown that their properties are comparable to wrought counterparts, there is no physical evidence that suggests CSAM of Al6061 will also exhibit similar characteristics [41].

Till date there is very limited literature and scientific understanding on CSAM of light metals such as titanium alloys [43,44] and aluminium alloy [45]. Moreover, these studies have employed CSAM systems that make use of helium or nitrogen as inert carrier gases for the printing process. This significantly adds to the costs of the printed parts. In a recent study, Hutasoit et al. [46] have reported using a modified CSAM system that utilises compressed air as the carrier gas. This system utilises heated compressed air to propel metal powder particles from a stationary nozzle onto a build plate clamped on a moving robot arm. Although this system has been successfully applied to printing copper parts, there is no literature that reports printing aluminium parts using similar CSAM setup. Therefore, one of the primary objectives of this study is to analyse the properties of CSAM-printed Al6061 parts in comparison with wrought counterparts.

It has been reported that there is significant anisotropy in metal parts printed in different orientations using laser-based AM techniques [9,11,47,48]. Similar anisotropic effects had been observed in copper parts printed using CSAM process [46,49,50]. Nonetheless, Hutasoit et al. [46] also reported that the degree of anisotropy in mechanical properties can be reduced and in some cases eliminated using an appropriate post-build heat treatment procedure. Therefore, one of the other objectives of this study is to investigate the effect of build orientation and post-build heat treatment on the microstructure, mechanical, and corrosion properties of Al6061 parts. To the best of the authors' knowledge, this work is the first to explore both the mechanical and corrosion properties of Al6061 alloy print-parts fabricated using this unique CSAM system.

## 2. Methodology

### 2.1. Materials

In this study, gas-atomised Al6061 powders with a chemical composition (measured by XRF) presented in Table 1 and particle size distribution between 5 µm and 60 µm (as specified by the powder supplier) was used. The morphology of the powder particles was studied using scanning electron microscopy (SEM), as shown in Fig. 1a. The powder comprised of a mixture of spherical and irregular shaped particles along with several satellite particulates. The composition of the wrought Al6061 plate (T6 temper treated) is also presented in Table 1.

### 2.2. Cold spray additive manufacturing process

Cold spray deposition was performed using a novel cold spray additive manufacturing (CSAM) system, where a stationary nozzle deposits metal powder on a substrate attached to the robot arm, as shown in Fig. 1b. During printing, a robot arm controlled by a built-in algorithm position the substrate in such a way that complicated geometry deposits can be manufactured. Prior to entering the nozzle, metal powder is mixed with heated high-pressure air, which facilitates sufficient ki-

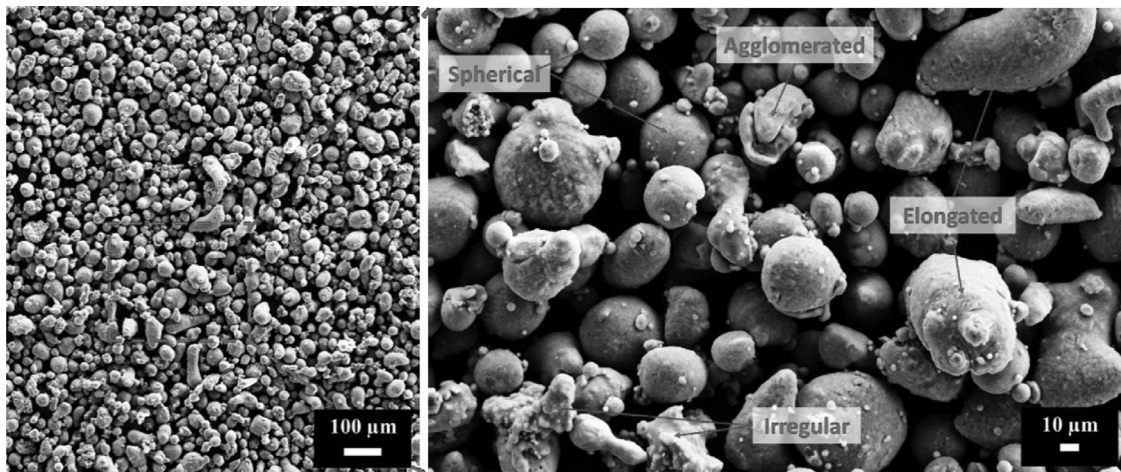


**Fig. 1.** (a) As-received Al6061 powders of size 5–60  $\mu\text{m}$  consisting of mixed morphology, (b) CSAM powder deposition system used in this study, consisting of a fixed nozzle for powder delivery and substrate on a movable robot arm.

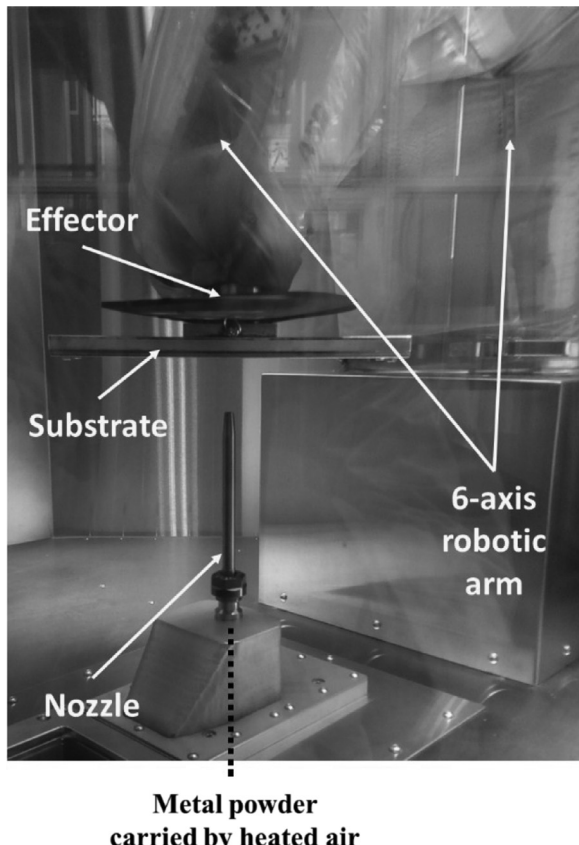


**Fig. 2.** Al6061 blocks cold-sprayed, (left) horizontally on XY-plane, and (right) vertically on XY-plane, printed with different dimensions for mechanical and corrosion testing.

netic energy in metal particles to generate adequate particle-substrate and particle-particle bonding strength after its impact with the substrate plate during deposition.

Al6061 powder was deposited on a 3 mm Al5005 substrate using 3 MPa compressed air pressure, nozzle exit temperature of 500 °C and stand-off distance between the nozzle and substrate plate maintained at 16 mm. Two groups of four blocks with different dimensions were manufactured as schematically shown in Fig. 2. The first group was used

**Table 2**  
List and notation of samples used in this study.

Condition	Sample code		
	As-received	As-deposited	Heat-treated
Wrought	W		
Cold-sprayed (horizontal)		CSH	CSH-T
Cold-sprayed (vertical)		CSV	CSV-T

for material and mechanical characterisation, while the second group was used for corrosion testing. To print these blocks, two printing sequences were employed that involved spraying at 45° and 90° angles, highlighted in Fig. 3a. During the process bulk of the inner region of the blocks were printed using a 90° spray angle (Fig. 3b), leaving around 3 mm edge regions across the part that was printed using a 45° spray angle (Fig. 3c). In the first sequence, the spraying path followed a 'zig-zag' pattern along the X-axis with a constant traverse speed of 100 mm/s (Fig. 3d), whereas the second sequence was printed linearly following the edge lines (Fig. 3e). The thickness of a single layer of the deposit was maintained at around 1.68 mm.

### 2.3. Heat treatment

Heat treatment was carried out on two blocks of each group. The heat treatment procedure involved sintering (610 °C for 5 hrs, followed by furnace cooling), solutionising (530 °C for 1 hr followed by water quenching), and ageing (160 °C for 4 hrs followed by air cooling). The notation of the as-deposited and heat-treated group for all the samples are presented in Table 2.

### 2.4. Material and mechanical characterisations

The samples for material characterisation were cross-sectioned from the cut section of the tensile test sample with reference to the building direction of the deposit (Fig. 4). The cut samples were wet ground with water-proof SiC papers to 2000 grit and polished with 9  $\mu\text{m}$ , 3  $\mu\text{m}$ , and 1  $\mu\text{m}$  diamond suspension, and finally by OP-S (0.02  $\mu\text{m}$ ). The polished samples were then etched with a reagent containing 60% NaOH and 40% distilled water to reveal its microstructure. Hardness measurement was conducted using Buehler Micromet 3 micro-Vickers hardness tester with a diamond indenter using 100 gf load with a dwelling time of 10 s at 15 random locations on XZ-plane and XY-plane for horizontally and vertically-built samples, respectively. Microstructure on XY, XZ and

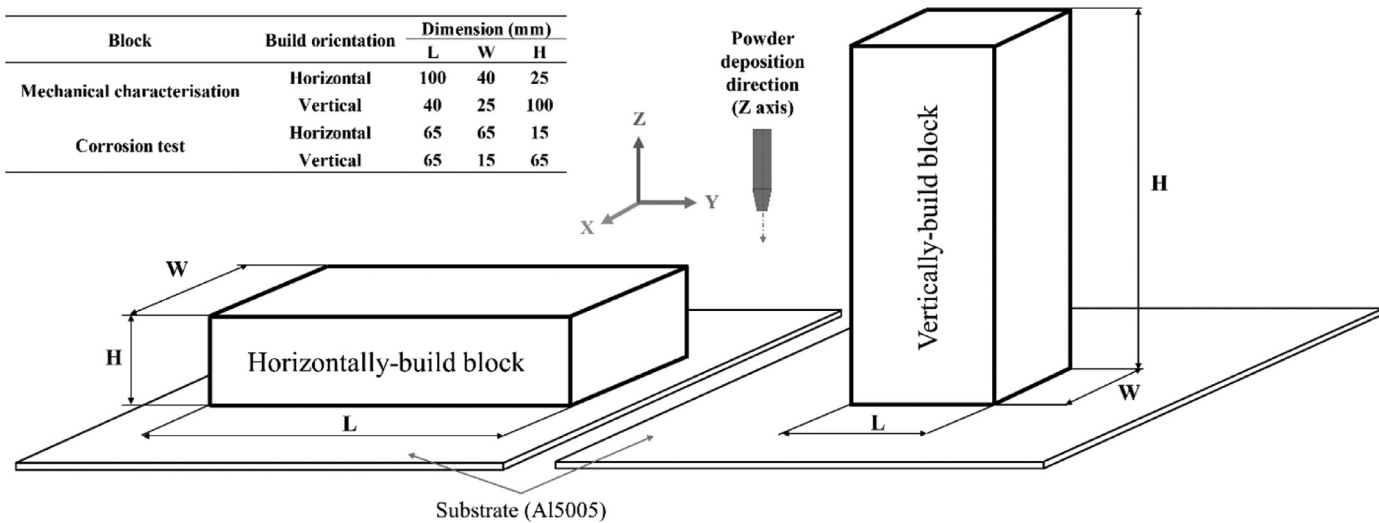


**Fig. 3.** Schematic illustration of the cold spray deposition process for (a) 45° and 90° spraying sequences, along (b) the core of the part, and (c) the edges of the part. (d) the printing is in a zig-zag pattern for a 90° spray, and (e) in linear path for a 45° spray angle.

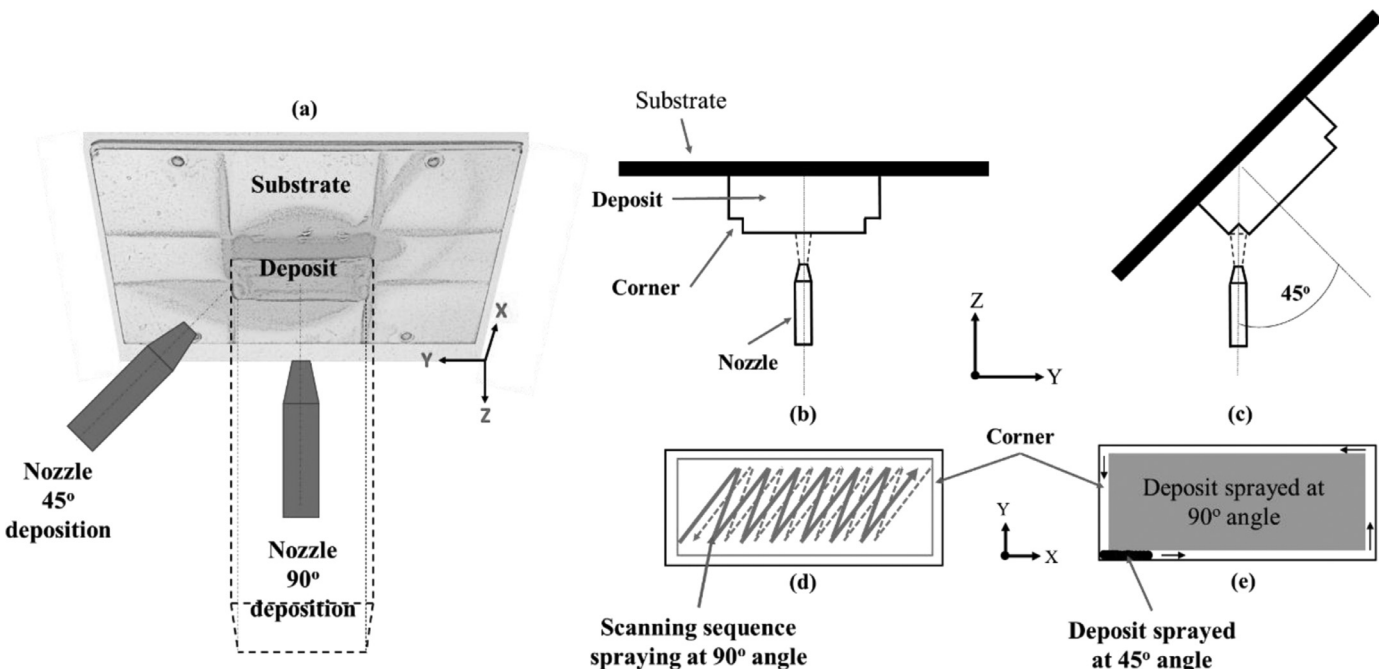


**Fig. 4.** Schematic illustration of the sectioned region (red shaded) for material characterisation that were cut from the printed blocks.

YZ-plane, and fracture mechanisms were analysed using ZEISS SUPRA 40VP SEM equipped with secondary and backscatter electron detectors.

As particle shape influences mechanical properties in powder metallurgy [51], this study assessed three particle shape descriptors on the strength of cold sprayed deposits. The descriptors are area, circularity - how close an object resembles a perfect circle), and aspect ratio (AR) - a ratio of the particles fitted ellipse. These parameters were calculated from the microstructure image obtained by SEM. Particle boundary was identified and rendered manually and subsequently detected by an image processing software (ImageJ) for calculating the three shape descriptors. Sphericity and aspect ratio is defined as follows:

$$\text{Circularity} = 4\pi \frac{\text{Area}}{\text{Perimeter}^2} \quad (1)$$

Circularity with a value of 1 indicates a perfect circle, whereas the value approaches 0, indicates an increasingly elongated shape

$$AR = \frac{\text{Major axis}}{\text{Minor axis}} \quad (2)$$

The higher AR value indicates a tendency to form an ellipse geometry

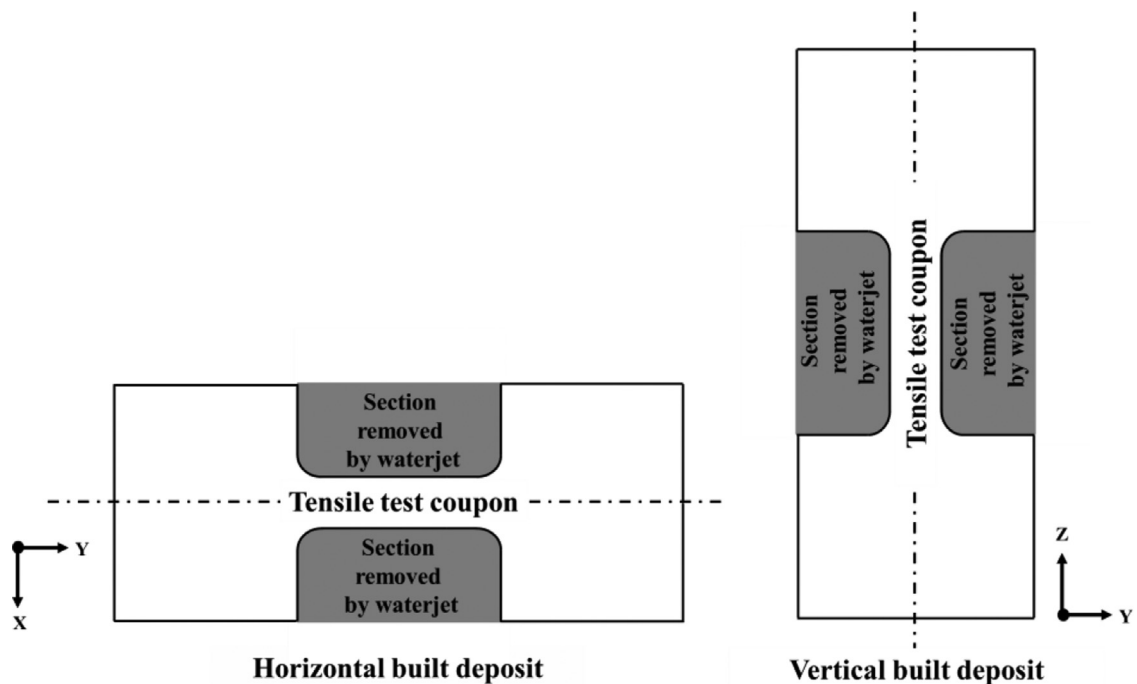
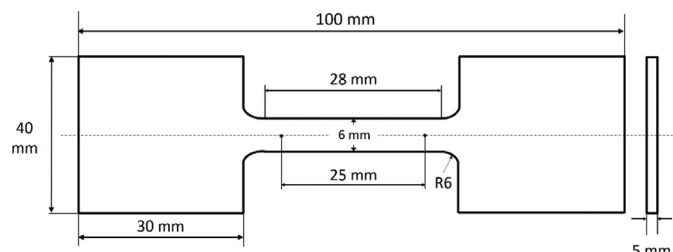
A Bruker D8 Advance XRD machine operated at 40 kV and 30 mA equipped with a graphite monochromator, a Ni filtered Cu K $\alpha$  ( $\lambda=1.5406$  nm) source, and a scintillation counter was used to obtain the XRD spectra for each sample. The phases of interest were Al and Mg<sub>2</sub>Si, as these were commonly found in Al6061 and reported in the literature [37]. A series of XRD scan was performed on XY and YZ-plane in horizontally-build (CSH and CSH-T) and vertically-built blocks (CSV and CSV-T), respectively.

For mechanical characterisation, three tensile test samples with dimensions shown in Fig. 5, were machined from the blocks. Tensile tests were carried out using MTS universal testing machine with a cross-head

**Table 3**

Chemical analysis of filtered, sterilised and pasteurised seawater used for corrosion tests .

pH	Conductivity µS/cm	Salinity (TDS) mg/L	Chlorides mg/L	Sulphate mg/L	Nitrates mg/L	Phosphate mg/L	TOC mg/L	Coliform MPN
7.7	50,000	32,500	18,000	2800	<0.05	0.06	7.9	<1

**Fig. 5.** The dimensions of the tensile test samples used in this study which conforms to ASTM E8 standard.**Fig. 6.** Photo of Al6061 coupons immersed in filtered seawater sourced from Port Melbourne, Australia.

strain rate of 2 mm/minute, equivalent to a strain rate of 0.08/min experienced by test samples. Loading direction during tensile tests was in Y-direction and Z-direction for horizontally and vertically-built samples, respectively, as shown in Fig. 4.

## 2.5. Corrosion testing

### 2.5.1. Sample preparation

Square samples with dimensions of 20 mm × 20 mm × 5 mm were cut from the wrought and cold-sprayed blocks (Fig. 2) for corrosion testing purpose using an automatic abrasive wheel cutting machine with water cooling. The surfaces of interest for corrosion testing were XY, and YZ-plane surfaces on horizontally-built (CSH and CSH-T) and vertically-built (CSV and CSV-T) samples, respectively. A 2 mm hole was drilled close to the edge of the samples through which nylon string was passed to hang the samples during immersion testing. The samples were manually wet ground from all sides successively with 220, 320, 500 and 1200 grit SiC grinding papers. After grinding, the samples were first

**Fig. 7.** SEM and OM images showing microstructure and porosity; (a-f) on different planes in the as-deposited (CSH), and (g-l) on different planes in the heat-treated (CSH-T), horizontally-built samples.**Table 4**

Porosity content in as-deposited and heat-treated samples measured on different planes.

Plane	Porosity (%)			
	CSH	CSH-T	CSV	CSV-T
XY	0.58 ± 0.23	0.26 ± 0.06	1.63 ± 0.57	0.30 ± 0.11
XZ	2.08 ± 0.21	0.88 ± 0.27	0.58 ± 0.19	0.19 ± 0.03
YZ	0.90 ± 0.18	0.07 ± 0.01	2.06 ± 0.40	0.05 ± 0.02

rinsed with water, then ultrasonically cleaned with ethanol and finally dried and stored in a desiccator. The average surface roughness of the grounded samples was determined using a 3D optical profilometer and found to be within the range of 0.55 ± 0.05 µm.

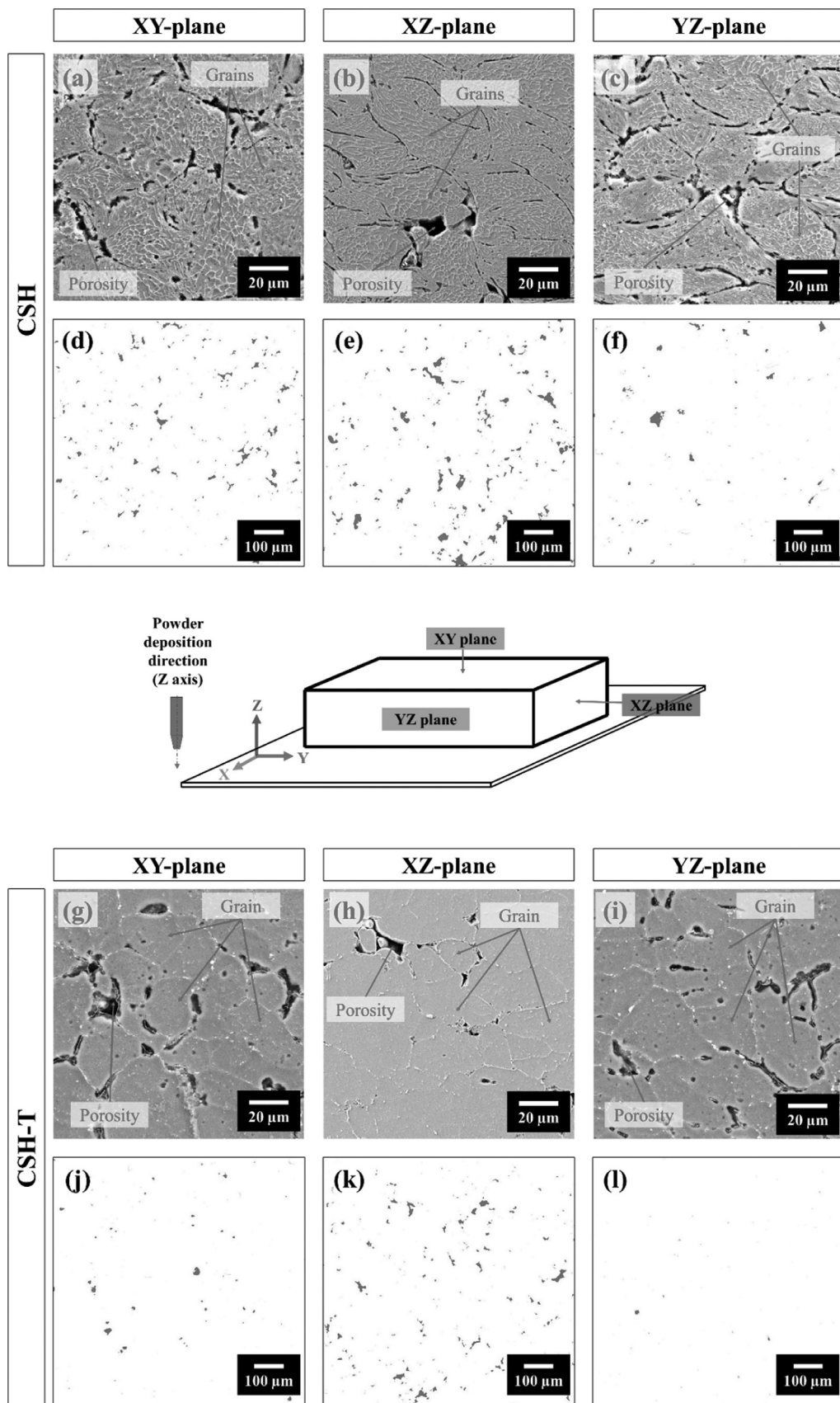


**Fig. 8.** SEM and OM images showing microstructure and porosity, (a-f) on different planes in the as-deposited (CSV), and (g-l) on different planes in the heat-treated (CSV-T), vertically-built samples.

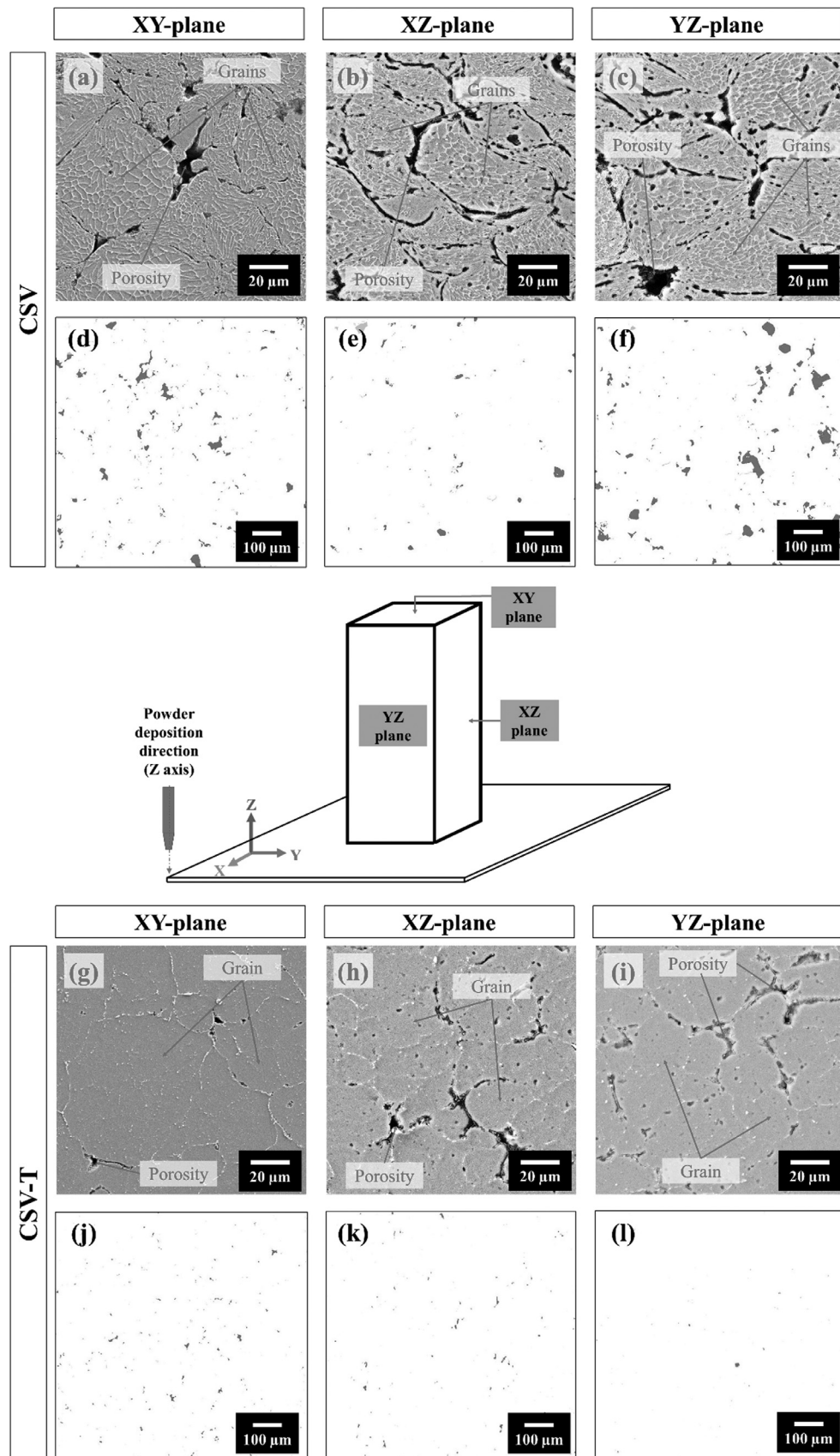


**Fig. 9.** Porosity in as-deposited and heat-treated samples. XZ-plane in CSH and XY-plane in CSV samples are the planes perpendicular to the loading direction during the tensile test and where hardness testing was performed.

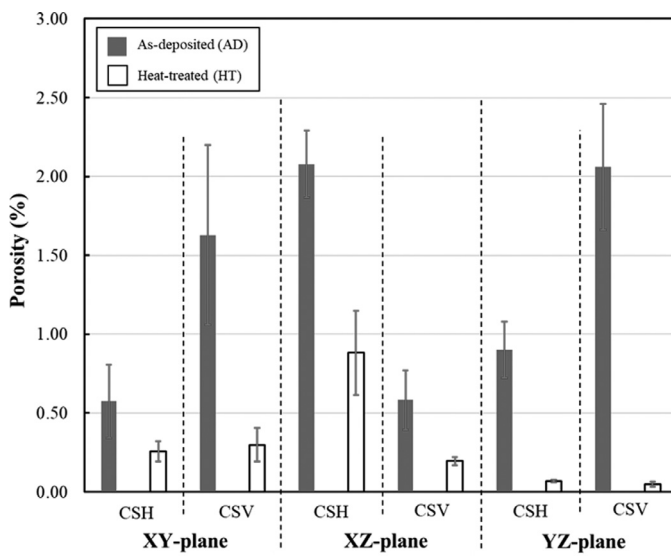


**Fig. 10.** Particle boundary tracing on (a) CSH-XY plane, (b) CSH-YZ plane. Particle descriptions and their relationship (c,d). The XY plane and YZ plane in CSH and CSV samples are planes perpendicular to the tensile loading direction. The deposition was performed in Z-direction.

#### 2.5.2. Immersion testing

The immersion test was carried out in seawater, which was collected from Station Pier, Port Melbourne, Victoria, Australia. The seawater was collected within the first metre of the water surface by immersing plastic containers (~10 litres capacity) by hand and filled to the top. Before immersion testing, the collected seawater was vacuum-filtered and sterilised via 0.02 µm pore filters and pasteurised by incubating at 70 °C for 2 h [52]. The filtration and pasteurisation of seawater were carried out to remove microbes, thereby facilitating abiotic corrosion. The chemical composition of the seawater was analysed from commercial vendor Eurofins, Melbourne and presented in Table 3.

Samples were tested in a glass bottle (~250 ml) which were filled with seawater. The samples were hung vertically with nylon string passing through the lid to fully immerse in seawater. A total of 9 samples of the five types of Al6061 samples were prepared, i.e. W, CSH, CSV, CSH-T, CSV-T, and immersed, as shown in Fig. 6. Three samples of each of the tested types were removed from the seawater after 20, 40 and 60 days of immersion and ultrasonically cleaned with 7% HNO<sub>3</sub> for 2 min each, then rinsed with ethanol and finally dried with N<sub>2</sub> gas.

#### 2.5.3. Pitting corrosion analysis

To observe the effect of corrosion, the surface morphology of the samples recovered from seawater immersion test at different time intervals were analysed via stereomicroscope, SEM and 3D optical profilometer. A detailed pit depth analysis on the surface of the samples was carried out using a 3D optical profilometer. Firstly, the entire surface of the samples was scanned to take an overview of the surface feature, then finally, images were recorded at areas with pits on the metal surface. For each metal sample, the pit morphology, distribution, depth and surface area were measured using VISION64™ software (v5.30, Bruker, Germany). The pit density was determined by counting the number of pits present on each scanned surface area. The maximum pit penetration rates were also evaluated using the average pit depths of ten deepest pits found on the surface of the samples.

#### 2.6. Statistical analysis

The numerical data were statistically evaluated using one-way analysis of variance with the help of statistical function available in Origin Pro 2018 software. The error bars used in the graphs indicate the stan-

dard error of the average value; the difference for which *p* values ≤ 0.05 were considered significant.

### 3. Results and discussion

The cold spray samples were printed in two different orientations (horizontal – CSH and vertical – CSV). One batch of these samples was heat-treated (CSH-T and CSV-T). Prior to mechanical testing, a detailed microstructural and porosity analysis was carried out as reported in the following section.

#### 3.1. Microstructure and porosity

Fig. 7 exhibits the microstructure and porosity in as-deposited and heat-treated horizontally-built blocks. The amount of porosity contained in these deposits is presented in Table 4 and Fig. 9. In the XY-plane in as-deposited condition (Fig. 7a), particles formed a ‘round’ morphology exposing the top section of the particle splats as they were deposited perpendicular to the XY-plane. However, on the XZ and YZ planes (parallel with deposition direction), particles tend to elongate along XY-plane (Fig. 7b,c) as a result of lateral flow stress during particle impact. This also deformed the grains within particles in the direction of flow stress such that they appear elongated. As-deposited samples, regardless of plane orientations, shows the evidence of porosity (Fig. 7d-f) caused by particle bridging and inter-particle gaps [53]. This type of porosity typically formed by low-velocity particles such that particles do not gain adequate kinetic energy for local plastic deformation during impact [39,40,54]; thus limit particles from flowing and filling voids generated by prior deposition. The distribution of porosity on different planes is presented in Fig. 7g-i. Heat-treated samples exhibited a significant metallurgical change. Metallurgical bonding between particles is observed as well as an increase in grain size (Fig. 7g-i). Also, a reduction in porosity after heat treatment regardless of plane references is evident (Fig. 7j-l) and corroborated by porosity volume fraction data (Table 4 and Fig. 9). This porosity is likely the remnant of inter-particle voids that are not filled by plastically-deformed particles during heat treatment.

Fig. 8 exhibits the microstructure and porosity in as-deposited and heat-treated vertically-built blocks. The amount of porosity contained in these deposits are presented in Table 4 and Fig. 9. On the XY-plane in as-deposited vertically-built samples (Fig. 8a), ‘round’ morphology particles, similar to the one in horizontally-built samples was observed. On the XZ and YZ planes (parallel with deposition direction), particles tend to elongate along XY-plane (Fig. 8b,c). As-deposited samples, regardless of plane orientations, shows the evidence of porosity (Fig. 8d-f). The distribution of porosity on different planes is presented in Fig. 8g-i. As observed in the horizontally-built samples, heat-treated vertically-built samples exhibited metallurgical bonding between particles and larger grain size (Fig. 8g-i), and a reduction in porosity (Fig. 8j-l), corroborated by the porosity volume fraction data (Table 4 and Fig. 9).

The higher amount of porosity in the as-deposited samples could be attributed to inter-particle gaps generated due to random size of the powder particles and irregular splat formation. However, when these samples were subjected to post-process heat treatment, the porosity decreased considerably. More so, the phases formed in the heat-treated samples could be different to those observed in the as-deposited condition.

Particle shape descriptors data is exhibited in Fig. 10. During the deposition, aluminium particles underwent a flattening process, thus showing a larger average area in the CSH-XY plane (Fig. 10a). In contrast, elongated particles tend to form on CSV-YZ plane (Fig. 10b). This also supported by particle shape descriptors, where lower average circularity and higher aspect ratio one in the CSV-YZ plane (Fig. 10c,d).

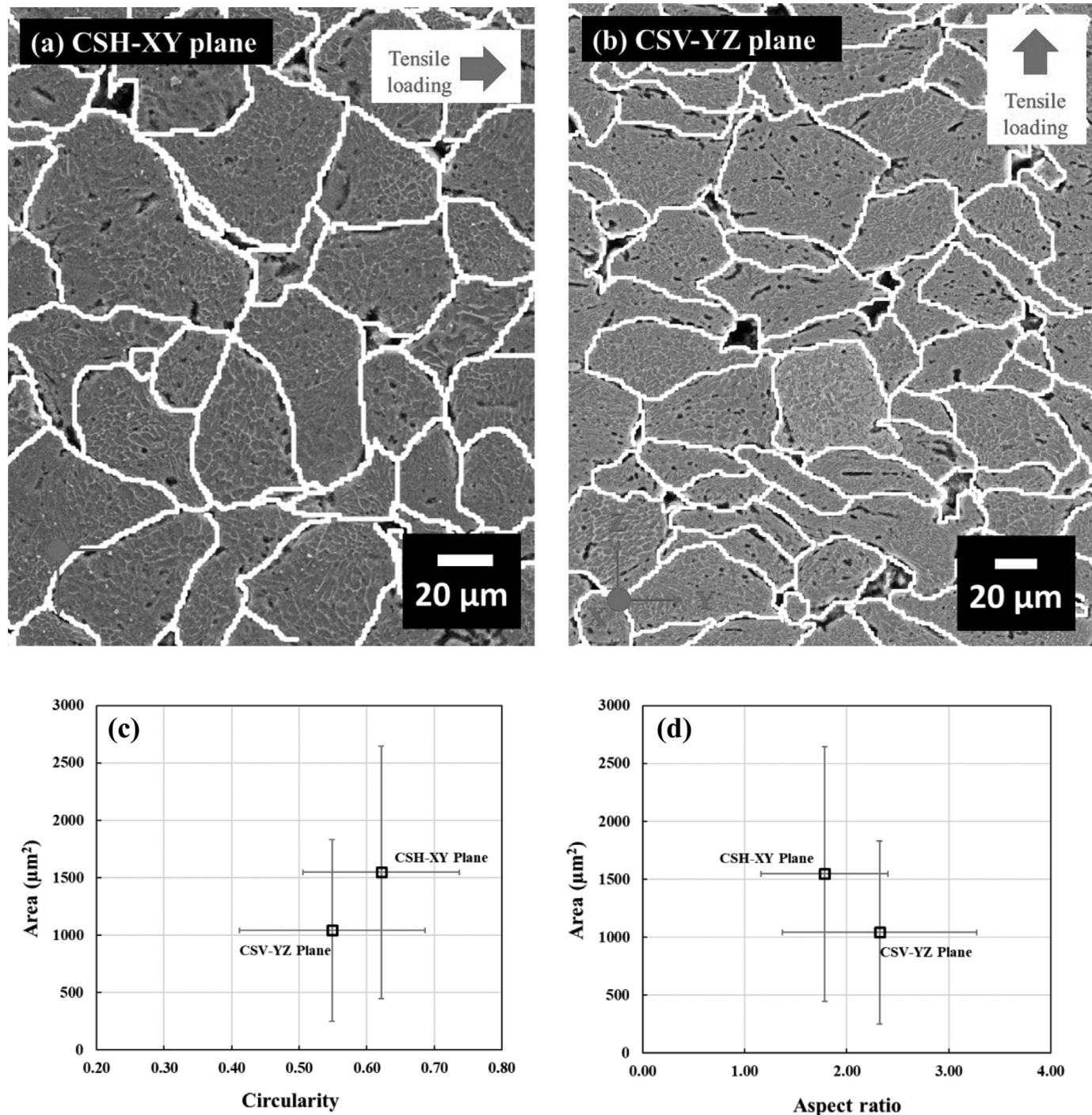


Fig. 11. XRD spectra of Al6061 in powder, wrought (W), as-deposited (CSH and CSV) and heat-treated (CSH-T and CSV-T) conditions.

### 3.2. X-ray diffraction

XRD spectra of the as-deposited and heat-treated samples are shown in Fig. 11. In this figure, all samples exhibited a consistent intensity peak angle ( $2\theta$ ) closest to the Al-FCC phase with crystallography open database (COD) ID 9008460 [55]. The intensity peaks of the precipitates, such as Mg<sub>2</sub>Si phase was not found in any of the samples studied. Precipitates were not detected primarily due to two plausible reasons. The low Si element content observed in the Al6061 powder was not sufficient to form Mg<sub>2</sub>Si precipitate, and therefore its presence was not

detected by the XRD scans [56]. Several studies [57,58] indicated that Si content of more than 0.6 was sufficient to form Mg<sub>2</sub>Si that precipitated in the inter-dendritic region between grains. Furthermore, precipitation treatment at 160 °C for four hours did not seem adequate to induce Mg<sub>2</sub>Si precipitates. This observation suggested that cold spray deposition and the subsequent heat treatment applied did not generate other phases, thereby resulting in the presence of predominantly Al (FCC) phase.

Following the metallurgical characterisation of the CSAM samples, it is evident that the primary difference in each condition is the amount of

**Table 5**  
Mechanical properties of wrought, as-deposited and heat-treated Al6061.

Sample code	Ultimate tensile strength (UTS) (MPa)	Fracture strain (%)	Hardness ( $\text{HV}_{0.1}$ )
W	307 ± 1	12.7 ± 0.4	110 ± 3
CSH	103 ± 8	0.3 ± 0.0	93 ± 15
CSV	78 ± 1	0.2 ± 0.0	84 ± 17
CSH-T	238 ± 17	6.1 ± 2.0	88 ± 4
CSV-T	241 ± 23	5.1 ± 3.8	96 ± 25

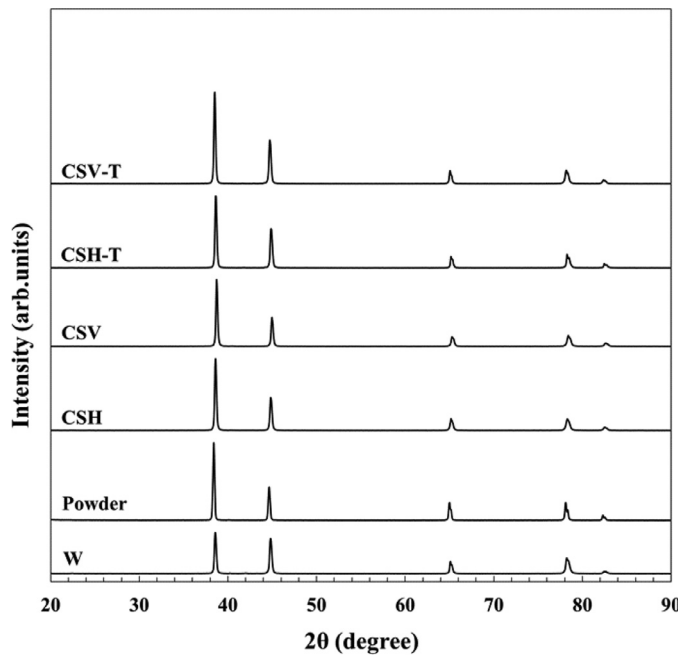


**Fig. 12.** Mechanical properties of wrought, as-deposited and heat-treated Al6061; (a) ultimate tensile strength and hardness on XZ-plane, (b) fracture strain and hardness on XZ-plane, and (c) hardness variations along different planes. XZ-plane and XY-plane are planes perpendicular to tensile loading direction in CSH and CSV samples, respectively..

porosity. There was no evidence to suggest microstructural variations due to different deposition orientations. The heat-treated samples appeared to show larger grains compared to the as-deposited condition. It has been proven in the literature that the differences in porosity and grain size can have a significant effect on the mechanical properties of the CSAM samples [46].

### 3.3. Mechanical properties and fracture behaviour

The mechanical properties of wrought, as-deposited and heat-treated Al6061 are presented in Table 5 and Fig. 12. Fractography of tensile test samples is presented in Fig. 13. In this study, regardless of build orientation, as-deposited samples exhibited the lowest ultimate tensile strength (UTS) and fracture strain compared to the ones in heat-treated and wrought condition (Fig. 12a,b). This is primarily due to the lack of metallurgical bonding between particles (Fig. 7a-c and Fig. 8a-c), leading to a low inter-particle bonding that promotes inter-particle fracture (Fig. 13a,e). Also, higher porosity content compared to the heat-treated condition may further reduce the deposit strength and strain, regardless of the build orientation. Porosity, in this case, acts as fracture initiation sites, resulting in brittle behaviour [59].

An interesting fact was observed when considering the effect of build orientation on the mechanical properties of deposits. Vertically-built deposits posed lower strength and fracture strain than horizontally-built deposits (Fig. 12a,b), although the two were manufactured using the

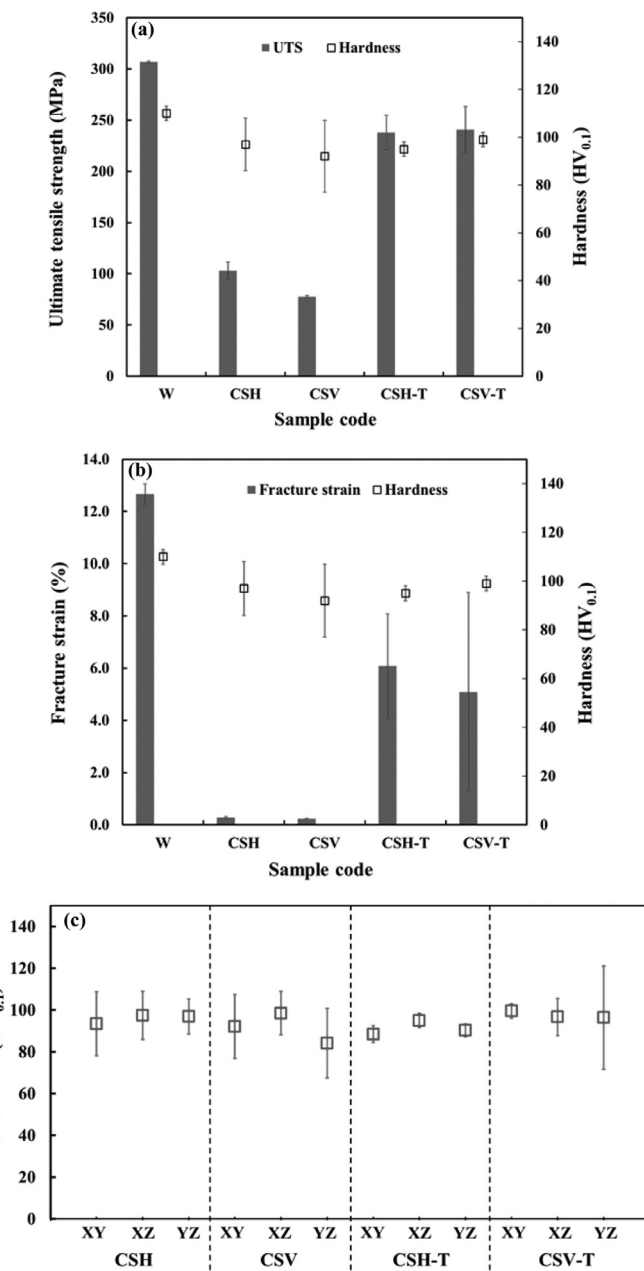


**Fig. 13.** (a-h) SEM images showing fracture surfaces of the tensile test samples, (i-j) schematic illustration of crack propagation in horizontally-built (CSH) and vertically-built (CSV) samples.

same cold spray process parameters. This can possibly be attributed to particle interlocking phenomenon. Cold spray deposition for CSH and CSV deposits was performed in the direction perpendicular to XY-plane such that impacted particles elongated along the XY-plane. However, since the two deposits were loaded with tension stress in different directions such as Y-axis and Z-axis for CSH and CSV samples, respectively,

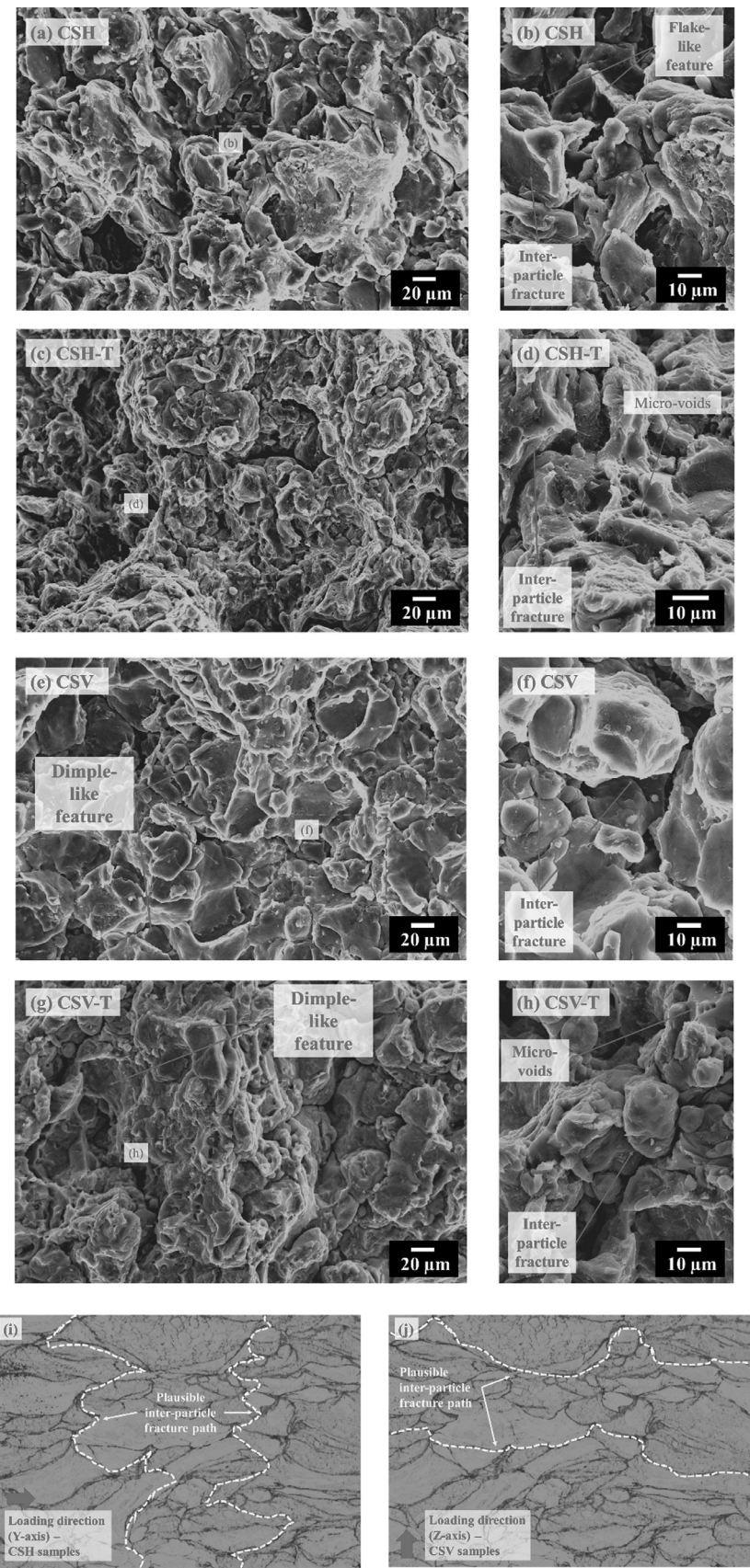


**Fig. 14.** Stereomicroscope images of samples (20 mm × 20 mm) after removal of corrosion products recovered after 20, 40 and 60 days of immersion in seawater.

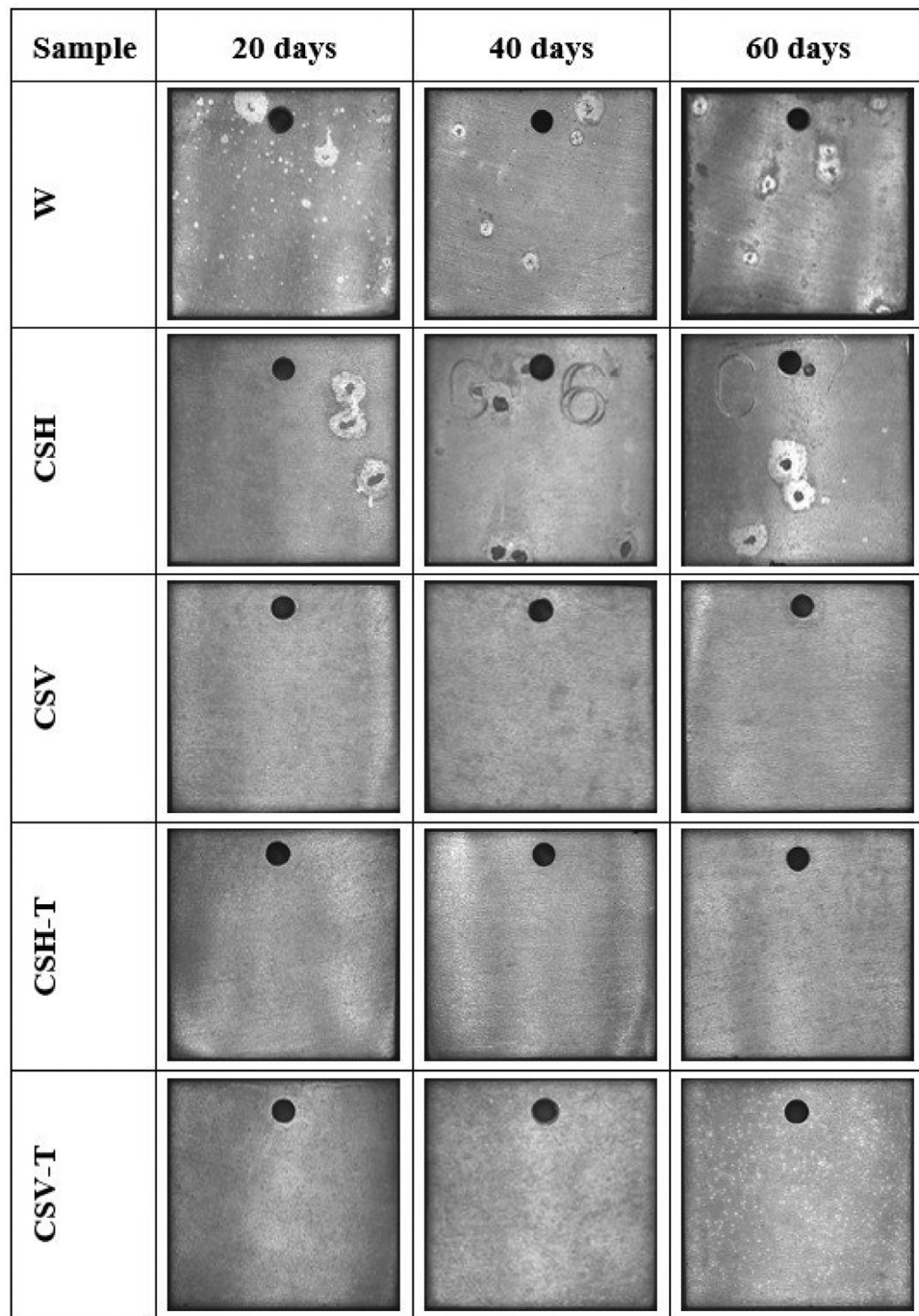


**Fig. 15.** Surface morphology of the samples showing similar surface features before corrosion testing .

particle shape may likely induce a particle-interlocking effect in the deposits. The CSV deposits are composed of smaller and more elongated particles (Fig. 10b) than those in the CSH counterpart (Fig. 10a). Subsequently, tensile loading (in the Z-axis direction) generates a particle peeling-off effect leading to inter-particle fracture. Upon inter-particle disintegration, a large particle surface area with a dimple-like feature formed (Fig. 13e,f), indicating less particle-interlocking effect. On the other hand, CSH deposits composed of larger particles and shape more resembling a trapezium (Fig. 10a). During tensile loading (in the Y-axis direction), these particle features may induce a higher particle-interlock effect indicated by particle shape descriptor (Fig. 10), leading to flake-like and tortuous fracture profiles (Fig. 13a,b), thereby improving tensile strength and fracture strain. This fact reinforces the findings of particle interlocking effect on the mechanical properties of objects manufactured by powder-based process technology [60,61]. A moderate variation in

hardness (Fig. 12c) was attributed due to variation in porosity on different planes (Fig. 9). This was observed in the as-deposited samples; however, it was considerably lower than the wrought samples (Fig. 12a,b).

Heat-treated samples exhibited a significant improvement in strength (2–3 times higher than as-deposited samples) and strain; however, they did not reach levels similar to the strength of the wrought counterparts (Table 5 and Fig. 12a,b). A similar trend was also reported in a study on cold spray aluminium by Rokni et al. [39]. These improvements can be elucidated by the formation of metallurgical bonding between particles (Fig. 7h and Fig. 8g) and a reduction in porosity (Fig. 9) induced by heat treatment. Micro-voids formed after decohesion of sintered particles was observed on the fracture surface of heat-treated samples (Fig. 13d,h), regardless of build orientation. The heat-treated samples showed improved strength and ductility which was evident with the micro-voids observed on the fracture surfaces (which indicates ductile

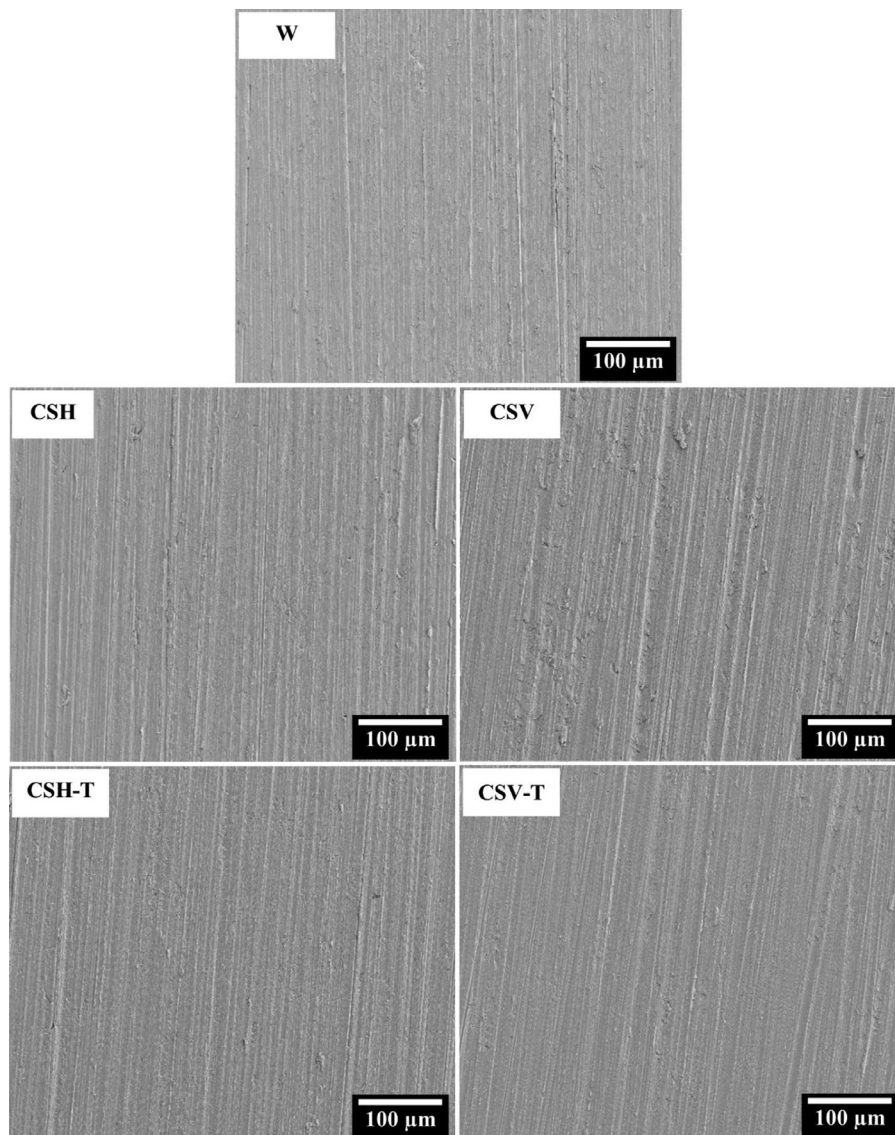


**Fig. 16.** SEM images showing examples of pitting corrosion attack on the surface of different tested samples at the end of 60 days of immersion in seawater.

deformation of the part). As the reduction in porosity after heat treatment is evident (Fig. 9), crack initiation sites were eliminated, thereby resulting in higher ductility.

It was interesting to observe absence of  $Mg_2Si$  precipitates in the heat-treated samples (Fig. 11), which may be due to insufficient ageing temperature ( $160\text{ }^{\circ}\text{C}$ ) and time (4 hrs). These secondary phase particles are important to induce precipitate strengthening effect, thereby resisting crack propagation in aluminium [62].

A slight increase in hardness of the heat-treated samples as compared to the as-deposited samples is likely contributed by a significant reduction in porosity that offset the ‘softening’ effect as a result of large and strain-free grains induced by heat treatment.

In terms of build orientation, heat treatment resulted in slightly higher strength and hardness in vertically-built samples compared to the ones in the horizontally-built samples (Fig. 13). As for strain, although heat-treated vertically-built samples showed a lower fracture strain compared to the horizontally-built, a large variation in strain in the two conditions was evident (Fig. 13b). This may suggest that the distribution of strain in the two build orientations are overlapped; thus, imply a tendency toward similar ductility. These facts suggest that the heat treatment cycle applied in this study was capable of eliminating the anisotropy effect induced by build orientation.

A direct mechanical properties comparison of additively manufactured Al6061 parts by different AM technologies is presented in Table 6. From this data, it can be inferred that the strength and ductility of as-deposited and heat-treated Al6061 examined in the current study are lower than those produced by selective laser melting (SLM) process. This difference can be attributed to the poor metallurgical bonding between particles in the CSAM process. Furthermore, it can be observed that the hardness of the SLM-printed Al6061 is considerably lower than the CSAM-printed samples. Further investigation is required to understand the mechanisms that govern the print-part properties in various AM processes.

Another interesting observation from Table 6 is the superior strength and hardness of Al6061 coatings produced using cold spray with helium as the carrier gas. This suggests that using inert gas as a carrier gas for metal powders in the CSAM process might induce enhanced mechanical performance [63]. In the current study, compressed air was used as the carrier gas, and this may likely generate insufficient particle velocity [64], thereby leading to poor bonding [65].

### 3.4. Corrosion behaviour

The variation in deposition orientation as well as post-process heat treatment had significant influence on the mechanical properties. More-

**Table 6**

Mechanical properties of additively manufactured Al6061 samples.

AM process	Condition	Tensile strength (MPa)	Yield Strength (MPa)	Fracture strain (%)	Hardness (HV)	Reference
SLM	As-built	133	66	–	54 ± 2.5	[18]
SLM	As-built	290 – 396.5	196 – 246.7	–	67 – 84	[19]
CS coatings (He carrier gas)	As-built	440	–	3.1	1.43–1.77 GPa	[38]
	Stress-relieved	490		3.6		
	T6	460		3.8		
CSAM (Air carrier gas)	As-built	78 – 103	–	0.2–0.3	84–93	Current study
	Solution and aged	238 – 241	–	5.1–6.1	88.96	

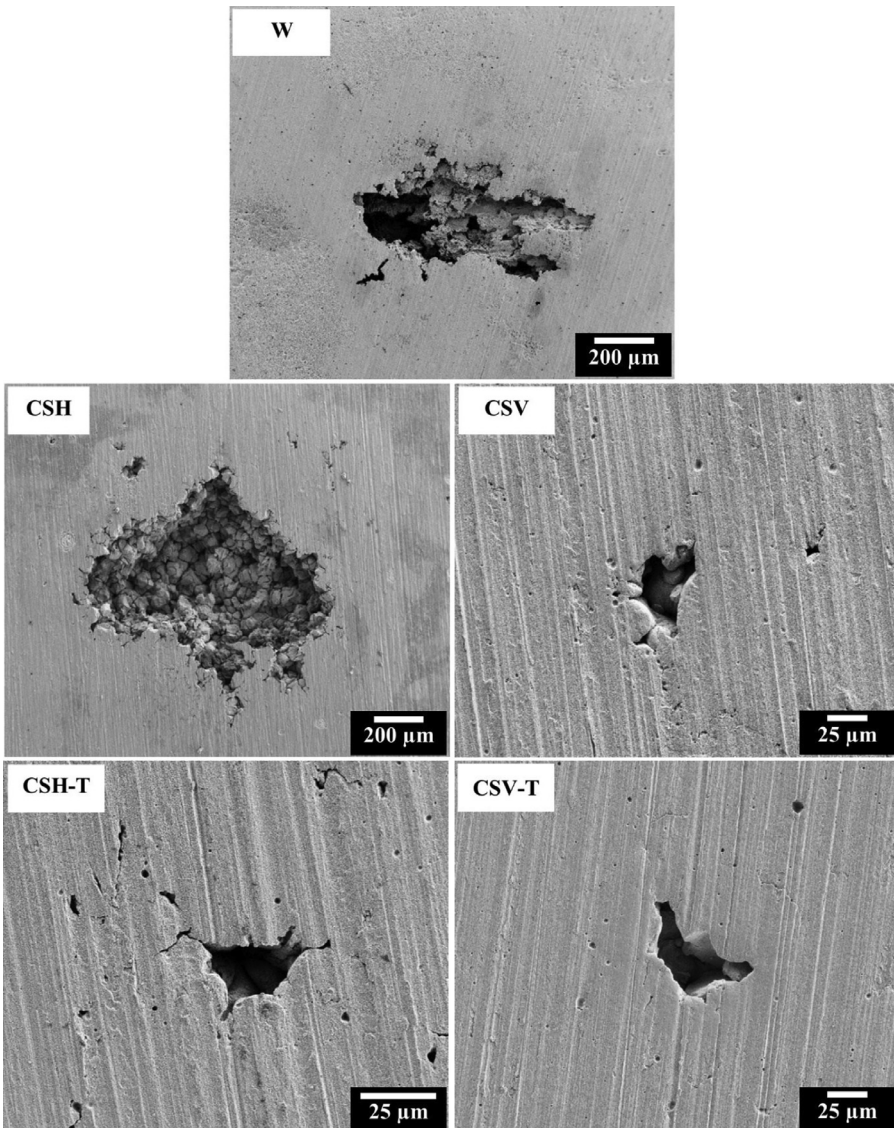


**Fig. 17.** Pitting corrosion attack on (a) wrought (W) and (c) as-deposited horizontal (CSH) samples ( $20 \times 20$  mm) recovered from seawater after 60 days, (b) and (d) 3d profiles showing morphology and depth of pits found on the surface of (a) W and (c) CSH, respectively.

over, the presence of porosities in the printed samples as well as the strain-hardened state of the grains can have deleterious effect on the corrosion performance of Al6061 components when put in service [66]. Hence, a detailed corrosion testing of these samples was carried out.

Stereomicroscope images of the samples retrieved from seawater after removal of corrosion products at different times of immersion, i.e. 20, 40 and 60 days, are shown in Fig. 14. Macroscale pits can be clearly seen on the surface of the wrought (W) and as-deposited horizontal (CSH) samples at each of the three-time points. In contrast, no such pits were visible on the rest of the samples, i.e. as-deposited vertical (CSV) and heat-treated CSH-T and CSV-T samples.

Fig. 15 shows an example of SEM images of freshly ground (1200 grit) sample of each of the five different types of samples tested. The surface of the samples showed vertical scratch marks which are typical morphology of the 1200 grit ground samples. Therefore, it is likely that any differences in surface corrosion phenomena of the samples is directly attributable to the sample process condition rather than the surface characteristics.

Fig. 16 shows SEM images of samples after 60 days of immersion in seawater. The images showed the macroscale pits on W and CSH samples, whereas micro-pits were found on the surface of rest of the tested sample types, i.e. CSH-T, CSV and CSV-T.

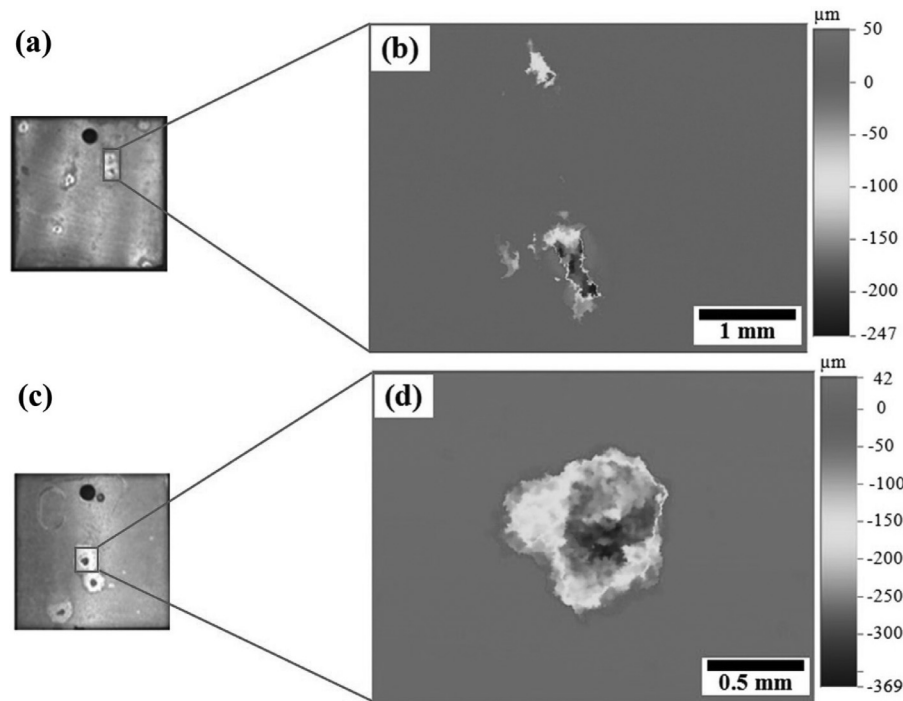


**Fig. 18.** Maximum pit penetration rate for wrought, as-deposited (CSH, CSV) and heat-treated (CSH-T, CSV-T) Al6061 samples immersed for 60 days in seawater

**Table 7**  
Pit depth data analysis of wrought, as-deposited and heat-treated Al6061 samples after 60 days of immersion in seawater.

Sample code	Pit density ( $\text{m}^{-2} \times 10^5$ )	Max. pit depth ( $\mu\text{m}$ )	Avg. of 10 deepest pits	
			Depth( $\mu\text{m}$ )	Surface area( $\text{mm}^2 \times 10^{-4}$ )
W	$8 \pm 2$	242	$129 \pm 27$	$2336 \pm 346$
CSH	$11 \pm 2$	396	$207 \pm 48$	$5671 \pm 2598$
CSV	$205 \pm 18$	59	$46 \pm 2$	$11 \pm 2$
CSH-T	$245 \pm 24$	71	$51 \pm 3$	$42 \pm 12$
CSV-T	$227 \pm 22$	57	$44 \pm 3$	$12 \pm 3$

The results of pitting corrosion analysis carried out for wrought, as-deposited and heat-treated Al6061 samples after 60 days of immersion using 3D optical profilometer are summarised in Table 7. The pitting data for the samples recovered after 20 and 40 days of immersion in seawater shows similar trends amongst different sample types tested (supplementary data Fig. 1s and 2s).

Photos of the cleaned wrought and as-deposited Al6061 samples showed a localised attack in the form of large pits (Fig. 17a,c). Fig. 17b,d represent 3D optical profilometer images of selected pits found on the surface of wrought and as-deposited Al6061 samples. Examples of 3D optical profilometer images of microscale pits found on the surface of as-deposited vertical (CSV), heat-treated horizontal (CSH-T) and vertical (CSV-T) Al6061 samples at the end of 60 days of immersion in seawater are shown in Fig. 3s.

The maximum pit penetration rate was calculated from 3D optical profilometer pit depth data for wrought, as-deposited and heat-treated Al6061 samples (Fig. 18). The results showed significantly greater ( $p > 0.05$ ) values for CSH compared to the other samples. The maximum pit penetration rate for CSH was 1.26 mm/y, which was found to be approximately 1.6×, 4.5×, 4.0× and 4.8× greater than W, CSV, CSH-T and CSV-T, respectively. The maximum pit penetration rate for CSV, CSH-T and CSV-T were all below 0.32 mm/y, and there was no significant difference present ( $p < 0.05$ ) between them. The overall trend observed in the maximum pit penetration rates for different tested samples is CSH > W > CSV ≈ CSH-T ≈ CSV-T.

CSH samples manifested the deepest pit depth (Table 7) and the maximum pit penetration rate (Fig. 18) during corrosion testing, com-

pared to all other samples tested. In terms of build-directions, horizontal build samples showed less resistance to pitting corrosion compared to vertically-built samples. This fact is plausibly contributed by the strain-hardened particles which experience deformation during deposition. Grains near the vicinity of the particle interface experience a higher strain hardening effect, thus, induces higher hardness compared to the ones in the inner region of the impacted particle [67,68]. Corroding surface (XY-plane) in horizontally-built samples (CSH) exhibited a larger particle cross-section area (Fig. 7a, 10a) and thus exposing more strain-hardened grains with higher residual stress leading to a higher hardness (Fig. 12c) compared to the one in vertically-built samples (CSV; YZ-plane) (Fig. 8c, 10b) [69]. Furthermore, exposing more strain-hardened particles to a corrosive environment increases the pitting corrosion rate since these are sites with high residual stresses and are prone to corrosive attack [70,71]. An interesting observation inferred from Fig. 9 and Fig. 18 is that the corroding plane (XY-plane) in CSH samples posed a lower porosity but manifested a higher corrosion rate compared to ones in CSV samples (YZ-plane). This suggests that the amount of porosity may not directly influence the corrosion property of cold-sprayed parts.

#### 4. Conclusion

This study investigated the mechanical and corrosion properties of Al6061 cold spray additively manufactured parts. In conclusion, the findings revealed in this current study suggests:

- 1) Regardless of build-orientations, as-deposited samples manifested the lowest ultimate tensile strength and ductility; caused by low inter-particle bonding strength. On the other hand, heat-treated samples showed improvements in strength and ductility to a level close to the ones in wrought condition.
- 2) Particle shape has a direct correlation with the strength of as-deposited, horizontally and vertically build. Particle shape descriptors in horizontally build samples may indicate a higher particle interlocking thus increase the strength of this sample compared to the one in vertically build condition.
- 3) Improvement in strength and ductility in the heat-treated samples was obtained mainly through sintering at 610 °C and solution treatment at 530 °C. Sintering forms inter-particle metallurgical bonding, while solution treatment induces strain-free grains. Precipitation hardening treatment at 160 °C for four hours was found inadequate to generate Mg<sub>2</sub>Si - precipitates responsible for hardening effect in Al6061. Extended studies are required to identify the optimum heat treatment route to further improve the mechanical properties of cold spray additively manufactured parts.
- 4) Horizontally-built samples showed the lowest pitting corrosion resistance compared to the vertically-built samples. This phenomenon plausibly caused by exposure of more strain-hardened particles in the horizontally-built samples to the corrosive environment.
- 5) Heat treatment improved the corrosion resistance of as-deposited samples, regardless of build orientation, to a level superior to the one in wrought condition. This increase was attributed to the formation of strain-free grains that are less susceptible to corrosion attack.

#### Author contributions

Novana Hutasoit: Conceptualization, Investigation, Methodology, Data curation, Formal analysis, Writing – original draft

Muhammed Awais Javed: Investigation, Data curation, Formal analysis, Writing – original draft

Rizwan Abdul Rahman Rashid: Conceptualization, Methodology, Supervision, Writing – review and editing

Scott Wade: Supervision, Project Administration, Writing – review and editing

Suresh Palanisamy: Supervision, Project Administration, Funding Acquisition, Writing – review and editing

#### Declaration of Competing Interest

None.

**The authors would like to acknowledge the Victorian Government Future Industries Sector Growth program, along with the industry, SPEE3D, in acquiring LIGHTSPEE3D. This research project was also supported by the DMTC Limited (Australia). The paper has been written in line with the intellectual property rights granted to research partners from the original DMTC project. The corrosion part of this research work was supported by the Defence Science Institute (DSI). We also acknowledge their contribution toward the final outcomes**

The authors would like to thank Mr Michael Culton and Ms Yeanette Lizama for their technical support during this research study.

#### Supplementary materials

Supplementary material associated with this article can be found, in the online version, at [doi:10.1016/j.ijmecsci.2021.106526](https://doi.org/10.1016/j.ijmecsci.2021.106526).

#### References

- [1] Miller WS, Zhuang L, Bottema J, Wittebrood AJ, De Smet P, Haszler A, Vieregge A. Recent development in aluminium alloys for the automotive industry. Mater Sci Eng: A 2000;280(1):37–49.
- [2] Zain-ul-abdein M, Nélia D. Effect of coherent and incoherent precipitates upon the stress and strain fields of 6xxx aluminium alloys: a numerical analysis. Int J Mech Mater Des 2016;12(2):255–71.
- [3] Ahmad Z. Chapter 10 - atmospheric corrosion. In: Principles of corrosion engineering and corrosion control. Oxford: Butterworth-Heinemann; 2006. p. 550–75.
- [4] Wahid MA, Siddique AN, Khan ZA. Aluminum alloys in marine construction: characteristics, application, and problems from a fabrication viewpoint. Marine Syst Ocean Technol 2020;15(1):70–80.
- [5] Yang Y, Cheng Y, Peng S, Xu L, He C, Qi F, Zhao M, Shuai C. Microstructure evolution and texture tailoring of reduced graphene oxide reinforced Zn scaffold. Bioactive Mater 2021;6(5):1230–41.
- [6] Yang Y, Song X, Li X, Chen Z, Zhou C, Zhou Q, Chen Y. Recent progress in biomimetic additive manufacturing technology: from materials to functional structures. Adv Mater 2018;30(36):1706539.
- [7] Ngo TD, Kashani A, Imbalzano G, Nguyen KTQ, Hui D. Additive manufacturing (3D printing): a review of materials, methods, applications and challenges. Compos Part B: Eng 2018;143:172–96.
- [8] Zocca A, Colombo P, Gomes CM, Günster J. Additive manufacturing of ceramics: issues, potentialities, and opportunities. J Am Ceram Soc 2015;98(7):1983–2001.
- [9] Rashid R, Masood SH, Ruan D, Palanisamy S, Rahman Rashid RA, Elambasseri J, Brandt M. Effect of energy per layer on the anisotropy of selective laser melted AlSi12 aluminium alloy. Additive Manuf 2018;22:426–39.
- [10] Ponnusamy P, Rahman Rashid RA, Masood SH, Ruan D, Palanisamy S. Mechanical properties of SLM-printed aluminium alloys: a review. Materials (Basel, Switzerland) 2020;13(19).
- [11] Ponnusamy P, Masood SH, Ruan D, Palanisamy S, Rashid R. High strain rate dynamic behaviour of AlSi12 alloy processed by selective laser melting. Int J Adv Manuf Technol 2018;97(1):1023–35.
- [12] Ponnusamy P, Masood SH, Ruan D, Palanisamy S, Rashid RAR, Mukhlis R, Edwards NJ. Dynamic compressive behaviour of selective laser melted AlSi12 alloy: effect of elevated temperature and heat treatment. Additive Manuf 2020;36:101614.
- [13] Drücker S, Schulze M, Ipsen H, Bandegani L, Hoch H, Kluge M, Fiedler B. Experimental and numerical mechanical characterization of additively manufactured Ti6Al4V lattice structures considering progressive damage. Int J Mech Sci 2021;189.
- [14] Rashid R, Masood SH, Ruan D, Palanisamy S, Huang X, Rahman Rashid RA. Topology optimisation of additively manufactured lattice beams for three-point bending test, Solid Freeform Fabrication. In: 2018: Proceedings of the 29th Annual International Solid Freeform Fabrication Symposium - An Additive Manufacturing Conference, SFF 2018; 2020. p. 635–45.
- [15] Jin N, Yan Z, Wang Y, Cheng H, Zhang H. Effects of heat treatment on microstructure and mechanical properties of selective laser melted Ti-6Al-4V lattice materials. Int J Mech Sci 2021;190.
- [16] Geng L, Wu W, Sun L, Fang D. Damage characterizations and simulation of selective laser melting fabricated 3D re-entrant lattices based on in-situ CT testing and geometric reconstruction. Int J Mech Sci 2019;157–158:231–42.
- [17] Weidmann J, Großmann A, Mittelstedt C. Laser powder bed fusion manufacturing of aluminum honeycomb structures: theory and testing. Int J Mech Sci 2020;180.
- [18] Uddin SZ, Murr LE, Terrazas CA, Morton P, Roberson DA, Wicker RB. Processing and characterization of crack-free aluminum 6061 using high-temperature heating in laser powder bed fusion additive manufacturing. Additive Manuf 2018;22:405–15.
- [19] Ahmed HM, Yi FX, Mohamed AE, Stephen CV. The effect of selective laser melting process parameters on the microstructure and mechanical properties of Al6061 and AlSi10Mg alloys. Materials (Basel) 2018;12(1):12.
- [20] Rahman Rashid RA, Mallavarapu J, Palanisamy S, Masood SH. A comparative study of flexural properties of additively manufactured aluminium lattice structures. In: Materials Today: Proceedings; 2017. p. 8597–604.
- [21] Louvis E, Fox P, Sutcliffe CJ. Selective laser melting of aluminium components. J Mater Process Technol 2011;211(2):275–84.
- [22] Ning J, Sievers DE, Garmestani H, Liang SY. Analytical modeling of part porosity in metal additive manufacturing. Int J Mech Sci 2020;172.
- [23] Yin S, Cavaliere P, Aldwell B, Jenkins R, Liao H, Li W, Lupoi R. Cold spray additive manufacturing and repair: fundamentals and applications. Additive Manuf 2018;21:628–50.
- [24] Hutasoit N, Kennedy B, Hamilton S, Lutnick A, Rahman Rashid RA, Palanisamy S. Sars-CoV-2 (COVID-19) inactivation capability of copper-coated touch surface fabricated by cold-spray technology. Manuf Lett 2020;25:93–7.
- [25] Li W, Yang K, Yin S, Yang X, Xu Y, Lupoi R. Solid-state additive manufacturing and repairing by cold spraying: a review. J Mater Sci Technol 2018;34(3):440–57.
- [26] Singh H, Sidhu TS, Kalsi SBS, Karthikeyan J. Development of cold spray from innovation to emerging future coating technology. J Brazilian Soc Mech Sci Eng 2013;35(3):231–45.
- [27] Meyer M, Lupoi R. An analysis of the particulate flow in cold spray nozzles. Mech Sci 2015;6(2):127–36.
- [28] Champagne VK. m. institute of materials, mining, the cold spray materials deposition process : fundamentals and applications. Cambridge: Woodhead Boca Raton : CRC Press; 2007.
- [29] Schmidt T, Gärtner F, Assadi H, Kreye H. Development of a generalized parameter window for cold spray deposition. Acta Mater 2006;54(3):729–42.
- [30] Ito K, Ogawa K. Effects of spark-plasma sintering treatment on cold-sprayed copper coatings. J Therm Spray Technol 2014;23(1):104–13.
- [31] Pattison J, Celotto S, Morgan R, Bray M, O'Neill W. Cold gas dynamic manufacturing: a non-thermal approach to freeform fabrication. Int J Mach Tools Manuf 2007;47(3):627–34.
- [32] Stoltenhoff T, Borchers C, Gärtner F, Kreye H. Microstructures and key properties of cold-sprayed and thermally sprayed copper coatings. Surf Coat Technol 2006;200(16):4947–60.

- [33] Wang H-T, Li C-J, Yang G-J, Li C-X. Cold spraying of Fe/Al powder mixture: coating characteristics and influence of heat treatment on the phase structure. *Appl Surf Sci* 2008;255(5):2538–44 Part 1.
- [34] Huang R, Sone M, Ma W, Fukanuma H. The effects of heat treatment on the mechanical properties of cold-sprayed coatings. *Surf Coat Technol* 2015;261:278–88.
- [35] Seo D, Ogawa K, Sakaguchi K, Miyamoto N, Tsuzuki Y. Parameter study influencing thermal conductivity of annealed pure copper coatings deposited by selective cold spray processes. *Surf Coat Technol* 2012;206(8):2316–24.
- [36] Partovi-Nia R, Ramamurthy S, Zagidulin D, Chen J, Jacklin R, Keech P, Shoemaker DW. Corrosion of cold spray deposited copper coating on steel substrates. *Corrosion* 2015;71(10):1237–47.
- [37] Rokni MR, Widener CA, Ahrenkiel SP, Jasthi BK, Champagne VR. Annealing behaviour of 6061 aluminium deposited by high pressure cold spray. *Surf Eng* 2014;30(5):361–8.
- [38] Rokni MR, Widener CA, Ozdemir OC, Crawford GA. Microstructure and mechanical properties of cold sprayed 6061 Al in As-sprayed and heat treated condition. *Surf Coat Technol* 2017;309:641–50.
- [39] Rokni MR, Widener CA, Champagne VK, Crawford GA. Microstructure and mechanical properties of cold sprayed 7075 deposition during non-isothermal annealing. *Surf Coat Technol* 2015;276:305–15.
- [40] Rokni MR, Widener CA, Nardi AT, Champagne VK. Nano crystalline high energy milled 5083 Al powder deposited using cold spray. *Appl Surf Sci* 2014;305:797–804.
- [41] Diab M, Pang X, Jahed H. The effect of pure aluminum cold spray coating on corrosion and corrosion fatigue of magnesium (3% Al-1% Zn) extrusion. *Surf Coat Technol* 2017;309:423–35.
- [42] Örnek C. Additive manufacturing – a general corrosion perspective, corrosion engineering. *Sci Technol* 2018;53(7):531–5.
- [43] Froes F. Titanium powder metallurgy: a review - part 2. *Adv Mater Process* 2012;170(10):26–9.
- [44] Vo P, Goldbaum D, Wong W, Irissou E, Legoux J-G, Chromik RR, Yue S. 22 - Cold-spray processing of titanium and titanium alloys. In: Qian M, Froes FH, editors. *Titanium powder metallurgy*. Boston: Butterworth-Heinemann; 2015. p. 405–23.
- [45] White BC, Story WA, Brewer LN, Jordon JB. Fatigue behavior of freestanding AA2024 and AA7075 cold spray deposits. *Int J Fatigue* 2018;112:355–60.
- [46] Hutasoit N, Rashid RAR, Palanisamy S, Duguid A. Effect of build orientation and post-build heat treatment on the mechanical properties of cold spray additively manufactured copper parts. *Int J Adv Manuf Technol* 2020;110(9–10):2341–57.
- [47] Rahman Rashid RA, Barr CJ, Palanisamy S, Nazari KA, Orchowski N, Matthews N, Dargusch MS. Effect of clad orientation on the mechanical properties of laser-clad repaired ultra-high strength 300 M steel. *Surf Coat Technol* 2019;380:125090.
- [48] Tang H, Huang H, Liu C, Liu Z, Yan W. Multi-Scale modelling of structure-property relationship in additively manufactured metallic materials. *Int J Mech Sci* 2021;194.
- [49] Yang K, Li W, Yang X, Xu Y, Vairis A. Effect of heat treatment on the inherent anisotropy of cold sprayed copper deposits. *Surf Coat Technol* 2018;350:519–30.
- [50] Yin S, Jenkins R, Yan X, Lupoi R. Microstructure and mechanical anisotropy of additively manufactured cold spray copper deposits. *Mater Sci Eng: A* 2018;734:67–76.
- [51] Miyake K, Hirata Y, Shimonosono T, Sameshima S. The effect of particle shape on sintering behavior and compressive strength of porous alumina. *Materials (Basel)* 2018;11(7):1137.
- [52] Little B, Gerchakov S, Udey L. A method for sterilization of natural seawater. *J Microbiol Methods* 1987;7(4):193–200.
- [53] Zahiri SH, Fraser D, Gulizia S, Jahedi M. Effect of processing conditions on porosity formation in cold gas dynamic spraying of copper. *J Therm Spray Technol* 2006;15(3):422–30.
- [54] Ajdelsztajn L, Schoenung JM, Jodoin B, Kim GE. Cold spray deposition of nanocrystalline aluminum alloys. *Metall Mater Trans A* 2005;36(3):657–66.
- [55] <http://www.crystallography.net/cod/>. <http://www.crystallography.net/cod/>.
- [56] Sabard A, Hussain T. Inter-particle bonding in cold spray deposition of a gas-atmosied and a solution heat-treated Al 6061 powder. *J Mater Sci* 2019;54(18):12061–78.
- [57] Revilla RI, De Graeve I. Influence of si content on the microstructure and corrosion behavior of additive manufactured Al-Si alloys. *J Electrochem Soc* 2018;165(13):C926–32.
- [58] Rubben T, Revilla RI, De Graeve I. Influence of heat treatments on the corrosion mechanism of additive manufactured AlSi10Mg. *Corros Sci* 2019;147:406–15.
- [59] Hutasoit N, Rashid RAR, Palanisamy S, Duguid A. Effect of build orientation and post-build heat treatment on the mechanical properties of cold spray additively manufactured copper parts. *Int J Adv Manuf Technol* 2020;110(9):2341–57.
- [60] Nakayama N, Horita M, Sakagami S, Miki H, Miyazaki T, Takeishi H. Effect of powder shape and size on mechanical properties of Al thin plate formed by compression shearing method at room temperature. *Procedia Eng* 2014;81:1163–8.
- [61] Sahoo B, Joseph J, Sharma A, Paul J. Particle size and shape effects on the surface mechanical properties of aluminium coated with carbonaceous materials. *J Compos Mater* 2019;53(2):261–70.
- [62] Maisonneuve D, Sury M, Nelias D, Chaudet P, Epicier T. Effects of heat treatments on the microstructure and mechanical properties of a 6061 aluminium alloy. *Mater Sci Eng: A* 2011;528(6):2718–24.
- [63] Binder K, Gottschalk J, Kollenda M, Gärtner F, Klassen T. Influence of impact angle and gas temperature on mechanical properties of titanium cold spray deposits. *J Therm Spray Technol* 2011;20(1):234–42.
- [64] Suo X, Yin S, Planché M-P, Liu T, Liao H. Strong effect of carrier gas species on particle velocity during cold spray processes. *Surf Coat Technol* 2015;268:90–3.
- [65] Ghelichi R, Bagherifard S, Donald DM, Brochu M, Jahed H, Jodoin B, Guagliano M. Fatigue strength of Al alloy cold sprayed with nanocrystalline powders. *Int J Fatigue* 2014;65:51–7.
- [66] Kumar S, Rao AA. Influence of coating defects on the corrosion behavior of cold sprayed refractory metals. *Appl Surf Sci* 2017;396:760–73.
- [67] Goldbaum D, Chromik RR, Yue S, Irissou E, Legoux J-G. Mechanical property mapping of cold sprayed Ti splats and coatings. *J Therm Spray Technol* 2011;20(3):486–96.
- [68] Zou Y, Goldbaum D, Szpunar JA, Yue S. Microstructure and nanohardness of cold-sprayed coatings: electron backscattered diffraction and nanoindentation studies. *Scr Mater* 2010;62(6):395–8.
- [69] Marzbanrad B, Jahed H, Toyserkani E. On the evolution of substrate's residual stress during cold spray process: a parametric study. *Mater Des* 2018;138:90–102.
- [70] Revilla RI, Liang J, Godet S, De Graeve I. Local corrosion behavior of additive manufactured AlSiMg alloy assessed by SEM and SKPFM. *J Electrochem Soc* 2016;164(2):C27–35.
- [71] Sander G, Tan J, Balan P, Gharbi O, Feenstra DR, Singer L, Thomas S, Kelly RG, Scully JR, Birbilis N. Corrosion of additively manufactured alloys: a review. *Corrosion* 2018;74(12):1318–50.